Simultaneous Intelligent Imaging of Nanoscale Reactivity and Topography by Scanning Electrochemical Microscopy

Dylan T. Jantz,[†] Ryan J. Balla,[‡] Siao-Han Huang,[‡] Niraja Kurapati,[‡] Shigeru Amemiya,[‡,*] and Kevin C. Leonard[†,*]

[†] Center for Environmentally Beneficial Catalysis, Department of Chemical and Petroleum Engineering, University of Kansas, 1501 Wakarusa Drive, Lawrence, Kansas 66047, United States.

[‡] Department of Chemistry, University of Pittsburgh, 219 Parkman Avenue, Pittsburgh, Pennsylvania, 15260, United States.

Emails. amemiya@pitt.edu, kcleonard@ku.edu.

ABSTRACT: Scanning electrochemical microscopy (SECM) enables reactivity and topography imaging of single nanostructures in the electrolyte solution. The in-situ reactivity and topography, however, are convoluted in the real-time image, thus requiring another imaging method for subsequent deconvolution. Herein, we develop the intelligent mode of nanoscale SECM to simultaneously obtain separate reactivity and topography images of non-flat substrates with reactive and inert regions. Specifically, an ~0.5 μm-diameter Pt tip approaches a substrate with an ~0.15 μm-height active Au band adjacent to an ~0.4 μm-wide slope of the inactive glass surface followed by a flat inactive glass region. The amperometric tip current versus tip–substrate distance is measured to observe feedback effects including redox-mediated electron tunneling from the substrate. The intelligent SECM software automatically terminates the tip approach depending on the local reactivity and topography of the substrate under the tip. The resultant short tip–substrate distances allow for non-contact and high-resolution imaging in contrast to other imaging modes based on approach curves. The numerical post-analysis of each approach curve locates the substrate under the tip for quantitative topography imaging and determines the tip current at a constant distance for topography-independent reactivity imaging. The nanoscale grooves are revealed by intelligent topography SECM imaging as compared to scanning electron microscopy and atomic force microscopy without reactivity information and as unnoticed by constant-height SECM imaging owing to the convolution of topography with reactivity. Additionally, intelligent reactivity imaging traces abrupt changes in the constant-distance tip current across the Au/glass boundary, which prevents constant-current SECM imaging.

Nanoscale scanning electrochemical microscopy (SECM) has emerged as a powerful method that can visualize the reactivity and topography of single nanometer-sized objects in the electrolyte solution.[1,2] For instance, the constant-height mode of SECM based on feedback effects[3] was used to image molecular transport through single solid-state nanopores with diameters of down to ~40 nm[4,5] and electrocatalysis at single metal nanoparticles with diameters of down to ~120 nm.[6,7] Constant-height imaging, however, suffers from the convolution of local reactivity and topography of substrate,[8] which was addressed by the separate measurement and analysis of SECM approach curves.[4-7] By contrast, the local reactivity of substrate can be resolved from topography by maintaining a constant tip–substrate distance during constant-current imaging,[9] which is straightforward only for the substrates that are relatively flat or uniformly reactive (or inert) as demonstrated by nanoscale SECM.[10,11] Alternatively, another imaging method can be combined with SECM[12] to obtain the topography image of single nanostructures in advance, which guides constant-distance reactivity imaging by SECM. The adoption of combined SECM techniques, however, has been limited[13] by the requirement of specialized hardware including a bifunctional probe and a dual probe for combination with atomic force microscopy[14] (AFM) and scanning ion-conductance microscopy,[15] respectively.

Herein, we advance the intelligent mode of nanoscale SECM[16] to simultaneously obtain separate reactivity and topography images of non-flat substrates with both reactive and inert regions. In the intelligent mode, the distance-dependent current response of an SECM nanotip is assessed after every step of the vertical tip approach to the substrate to achieve a short tip–substrate distance, d, without contact, thereby maximizing the spatial resolution based on feedback effects as represented by[17]

$$h^{\infty} = 1.5d + a \quad (1)$$

where h^{∞} is the radius of local substrate surface seen by a disk-shaped tip with a radius of a. Previously, we employed non-flat inert substrates to demonstrate that the intelligent mode enables non-contact topography imaging with a high resolution of $h^{\infty} \leq 1.45a$ with $d \leq 0.3a$ in eq 1[16] in contrast to other imaging modes based on approach curves, i.e., intermittent-contact[18] and hopping ($h^{\infty} = 8.5a$ with $d = 5a$[19]) modes. In this study, we reinforce the intelligent mode by the numerical post-analysis of each approach curve to locate the substrate under the tip for quantitative topography imaging and determine the tip current at a constant distance for topography-independent reactivity imaging.

Experimentally, we demonstrate the unprecedented power of the intelligent mode by resolving simultaneous changes in reactivity and topography at the grooved boundary between flush glass and Au surfaces of an interdigitated electrode (Figure 1). While the respective surfaces exert only negative or positive feedback effects on a tip (Figures 1A and 1B), the tip experiences both effects over the boundary to yield the mixed feedback current response (Figure 1C). Abrupt

changes in the mixed feedback current across the boundary can not be monitored by the constant-current mode[9] but are resolved by the intelligent mode to yield a topography-independent reactivity image. Moreover, intelligent topography imaging reveals the nanoscale grooves, which are comparable to topography imaging by scanning electron microscopy (SEM) and AFM without reactivity information and are unnoticed by constant-height imaging owing to the convolution of topography with reactivity. Moreover, we propose the new feedback mechanism based on long-range electron tunneling mediated by redox molecules,[20] which suddenly enhances the tip current to enable non-contact tip positioning over the non-flat Au/glass boundary.

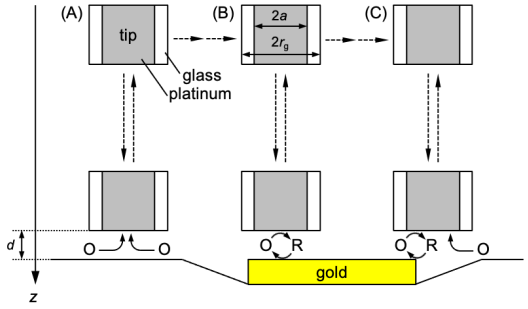

Figure 1. Scheme of tip approach for (A) negative, (B) positive, and (c) mixed feedback effects for intelligent SECM imaging of a Au band on a grooved glass substrate under a disk-shaped Pt nanotip with a thin glass sheath. Dashed lines with arrows indicate the tip movement. O and R are the oxidized and reduced forms of a redox mediator, respectively.

EXPERIMENTAL SECTION

SECM. A home-built SECM instrument was equipped with a potentiostat (CHI 802D, CH Instruments, Austin, TX) and controlled by using the Labview program based on a custom fuzzy logic algorithm as reported previously.[16] In addition, an SECM stage was accommodated in an isothermal chamber equipped with heat sinks and vacuum insulation plates to minimize thermal drift.[21] Pt tips were fabricated by laser-assisted pulling, heat annealing, and focused-ion-beam (FIB) milling and characterized by scanning electron microscopy (SEM) before and after use for SECM experiments to check the damage of the tips.[16] The tips were protected from electrostatic discharge as described in Supporting Information. Interdigitated Au electrodes on glass substrates (012260) were obtained as substrates from CH Instruments. Pt wires served as counter and quasi-reference electrodes. The tip potential was set to obtain the steady-state current based on the diffusion-limited reduction of 10 mM $Ru(NH_3)_6Cl$ (Strem Chemicals, Newburyport, MA) in 1 M KCl (≥99%, Sigma Aldrich, Milwaukee, WI) as prepared from Milli-Q water with the resistivity of 18.2 MΩ·cm and the total organic carbon of 2–3 ppb.

RESULTS AND DISCUSSION

Topography of Interdigitated Au Electrodes. We employed SEM (Figures 2A–C) and AFM (Figure 2D) to characterize the topography of interdigitated Au electrodes. A part of the Au band and the surrounding was removed by FIB milling (Figure 2B) to show an ~0.4 μm-wide groove of the glass surface at each side of the Au band (Figure 2C). The glass surface beyond the groove is flush with the gold surface as confirmed by AFM (Figure 2D). The AFM image also shows the asymmetric curvature of the Au surface, which widens a groove (right) more than the groove at the opposite side of the Au band (left). The asymmetry is not a hysteresis or any artifact, and is independent of the scan direction and observable by non-contact steady-state SECM imaging (see below). The grooves in the SEM image (~0.15 μm in Figure 2C) are deeper than those in the AFM image (~0.1 μm in Figure 2D), which is limited by the tip–substrate convolution.[22]

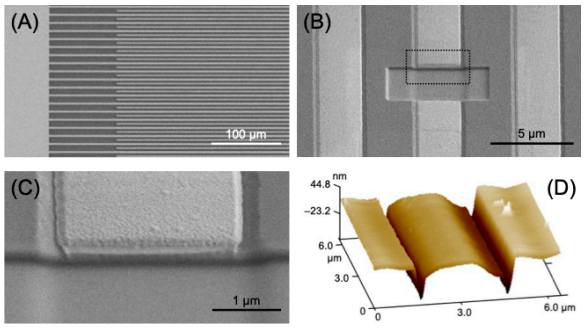

Figure 2. SEM images of (A) Au bands embedded in a glass substrate, (B) a Au band milled by FIB, and (C) the cross-section surrounded by the dotted line in part (B). (D) AFM image of non-milled Au band.

Theoretical Approach Curves. We performed the finite element simulation (see Supporting Information) to understand distance-dependent feedback effects on the amperometric current response of an SECM tip over a reactive band on a grooved inert substrate, which mimics the interdigitated electrodes (Figure 2). In the simulated approach curves (Figure 3), the tip–substrate distance, d, and the tip current, i_T, were normalized against the tip radius, a, and the tip current in the bulk solution, $i_{T,\infty}$, respectively. The latter is given by

$$i_{T,\infty} = 4xnFDc_0a \qquad (2)$$

where x is a function of RG (= r_g/a =~1.5; r_g is the outer tip diameter), n is the number of the transferred electrons, and D and c_0 are the diffusion coefficient and concentration of the redox mediator in the solution. Experimentally, simulation is required only after imaging experiments to analyze approach curves for the quantitative resolution of reactivity and topography images.

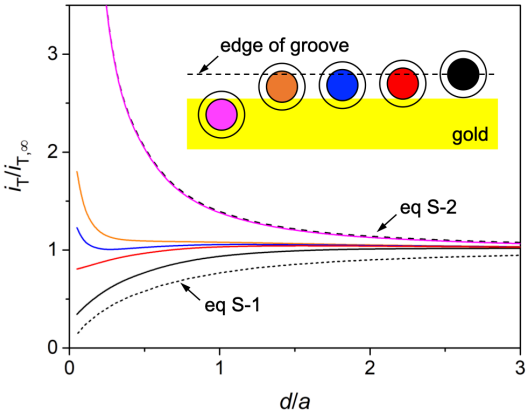

Figure 3. Theoretical approach curves (solid lines) simulated at various lateral tip positions over a Au band as depicted in the inset (top view) by using the same colors. Dotted and dashed lines represent diffusion-limited negative and positive curves, respectively.

The finite element simulation demonstrated that approach curves over the grooved boundary between Au and glass regions are highly sensitive to the lateral position of the tip owing to mixed feedback effects from both regions (Figure 1C). When the entire surface of the Pt tip is located over a Au band (purple tip in the inset of Figure 3), the resultant current (purple line) was most positive to follow the diffusion-limited positive approach curve (black dashed line). Interestingly, the approach curve changed from monotonically positive (orange line), positive, negative, and then positive (blue line), and monotonically negative (red line) as the lateral tip position was changed only by 10% of the tip radius over the boundary. The approach curve with both positive and negative feedback regions (blue line) yielded a characteristic maximum around d/a = 1.5, which uniquely fitted with an experimental approach curve to identify the corresponding lateral position of the substrate (see below).

The finite element simulation also illustrated how the inert groove at the boundary can be detected by intelligent topography imaging but not by widely used constant-height imaging. When the tip approaches the insulating groove, the tip current is greater than expected from a pure negative feedback effect from a flat surface, which is attributed to the diffusion of redox molecules from the recessed groove. Subsequently, the tip approaches closer to the groove to suppress the tip current until the tip current reaches a threshold preset for negative approach curves (e.g., <0.40$i_{T,\infty}$; see below). By contrast, the insulating groove is missed in the constant-height mode, where the tip is scanned at a constant height from the flush Au and glass surfaces to observe a monotonic change of the tip current over the grooved boundary from positive feedback current to negative feedback current or vice versa (e.g., d/a = 0.3 in Figure 3).

Imaging Algorithm. We developed a new algorithm for non-contact and high-resolution intelligent imaging of mixed reactive and inert substrates by considering characteristic approach curves, which were simulated theoretically (Figure 3) and confirmed experimentally (see below). With this algorithm, the tip approach at a flat reactive or inert region is terminated at a short tip–substrate distance of d/a = 0.3, which yields tip currents of ~3.0$i_{T,\infty}$. (black dashed line in Figure 3) and ~0.40$i_{T,\infty}$ (black dotted line), respectively, to represent substrate reactivities at the constant distance. These preset values, however, can not be reached for the tip current when the tip approaches the boundary (red, blue, and orange lines), thereby requiring different conditions for the non-contact tip approach. Specifically, the tip approach is terminated without the tip–substrate contact when a mildly negative approach (red line) significantly deviates from the diffusion-limited negative curve (black dotted line). This algorithm was successfully used for the intelligent imaging of insulating steps in our previous work[16] (see eq S-16).

In this work, we implemented two new conditions to terminate the tip approach to the boundary without contact when the tip current is enhanced mildly and monotonically (orange line in Figure 3) or inverted (blue line). In the latter, the tip approach is terminated when the tip current goes below the maximum value, $i_{T,max}$, by a present value, $\Delta i_{T,max}$, to yield

$$\Delta i_{T,max} < i_{T,max} - i_T \quad (3)$$

as demonstrated experimentally (Figure S-5). By contrast, the termination of the tip approach is challenging when the tip current is enhanced only mildly by a positive feedback effect from the reactive side of the boundary (orange line). This challenge, however, can be overcome by detecting a sudden increase in the tip current as found experimentally and attributed to long-range electron tunneling mediated by redox molecules (see below). Subsequently, the tip approach is terminated when the slope of the positive approach curve exceeds a preset value, m_{max}, as given by

$$m_{max} < \Delta i_n/\Delta z_n \quad (4)$$

where Δi_n and Δz_n represent changes in tip current and vertical tip position, respectively, after the nth step of the tip approach.

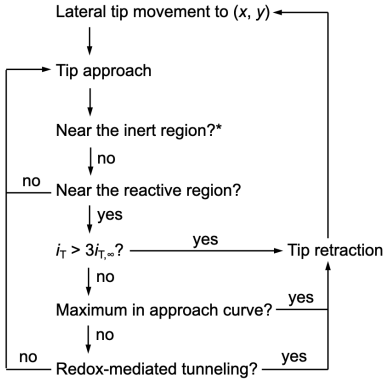

Figure 4. Flow chart of real-time assessment of approach curve. * See text for the algorithm when the tip approaches the inert region.

Overall, five conditions for the termination of tip approach were implemented in a new algorithm for non-contact intelligent imaging of mixed reactive and inert substrates (Figure 4). In this algorithm, the tip current is measured and assessed after each step of the tip approach to decide whether the tip–substrate distance is short enough to enhance or suppress the tip current, e.g., $i_T > 1.02i_{T,\infty}$ or $i_T < 0.98\ i_{T,\infty}$, respectively. Otherwise, the tip approaches one step closer to the substrate. If the tip current is suppressed sufficiently, the tip approach is terminated when the tip current reaches a threshold value, e.g., ~0.40$i_{T,\infty}$, or deviates from the pure negative feedback current (eq S-16).[16] Alternatively, the tip approach is terminated when the tip current reaches a preset value, e.g., ~3.0$i_{T,\infty}$, by the positive feedback effect, goes below the maximum by a preset amount (eq 3), or increases abruptly by redox-mediated electron tunneling (eq 4).

It should be noted that the proposed algorithm is applicable only to diffusion-limited negative and positive feedback effects (eqs S-1 and S-2, respectively[23]) in this work but will be extendable when a substrate reaction is controlled by electron-transfer kinetics. Specifically, a theoretical approach curve based on the kinetically controlled substrate reaction is given by an analytical equation[23] (eq S-5) and will be compared with an experimental approach curve after each step of tip approach to determine the tip–substrate distance and the electron-transfer rate constant for topography and reactivity imaging, respectively. The tip approach will be terminated without the tip–substrate contact when the tip–substrate distance reaches a threshold value, e.g., d/a = 0.3.

Deconvolution of Nanoscale Reactivity and Topography. We applied the intelligent mode by scanning a tip over interdigitated Au electrodes to separately obtain nanoscale reactivity and topography information. In this line scan experiment, we aimed at observing five characteristic approach curves at short tip–substrate distances as predicted theoretically (Figure 3). Accordingly, the tip approach to the boundary was not terminated by the deviation of the negative approach curve from the theoretical curve (eq S-16) or the maximum of approach curve (eq 3), where the tip was still relatively far

from the substrate. In the respective cases, the tip approach was terminated when the tip–substrate contact was detected by assessing a change in the slope of the negative portion of the approach curve as reported previously[16] (see eq S-17) or when the tip current was enhanced suddenly by redox-mediated electron tunneling (eq 4).

The amperometric tip current based on the diffusion-limited reduction of $Ru(NH_3)_6^{3+}$ was stable during the 13 minutes-long line scan with a lateral step size of 0.1 μm to obtain 61 approach curves including five characteristic approach curves (Figure 5). Specifically, the tip current reached the preset thresholds of ~$0.4i_{T,\infty}$ and ~$3.0i_{T,\infty}$ (e.g., curves 1 and 2, respectively) whenever the entire surface of Pt tip approached glass or Au surfaces, respectively. Interestingly, an approach curve with a maximum was also observed (curve 3) as expected theoretically when the tip approached the boundary. When the tip approached closer to the Au side of the boundary, the tip current increased monotonically to exceed the preset threshold of ~$3.0i_{T,\infty}$ owing to redox-mediated electron tunneling as exemplified by curve 4 and discussed below. By contrast, the tip experienced a mild negative feedback effect from the groove (e.g., curve 5) to contact the substrate without reaching the preset threshold of ~$0.4i_{T,\infty}$ when the tip approached closer to the glass side of the boundary.

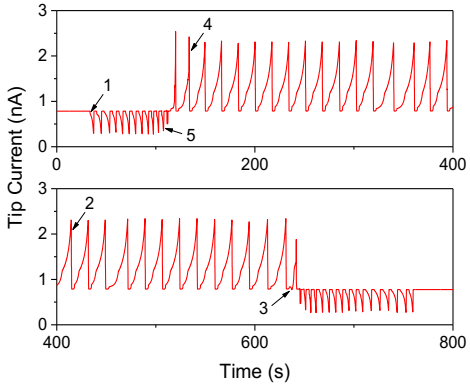

Figure 5. The tip current during line scan based on tip approach to Au and glass regions in 10 mM $Ru(NH_3)_6^{3+}$ and 1 M KCl. The outer and inner tip radii of 0.39 μm and 0.24 μm, respectively, were determined by SEM. Arrows indicate characteristic approach curves analyzed in Figure 8.

In the intelligent mode, the topography of the interdigitated Au electrode was obtained to reveal nanoscale grooves at both sides of a Au band. The grooves were observed by plotting the vertical tip position against the lateral tip position where the tip approach was terminated (blue circles in Figure 6A). Moreover, the actual positions of the substrate surface under the tip were determined (red circles in Figure 6B) by fitting experimental approach curves with eqs S-1 and S-2 over flat glass and Au surfaces, respectively, and also with simulated curves over the boundaries (see below). Both intelligent topography plots resemble the corresponding AFM topography (black dashed lines) including not only the width of the Au band (~2.8 μm as indicated by vertical dotted lines) but also the deeper recession of the Au surface at the lateral tip positions between 3 μm and 4 μm, which represents the remarkably high sensitivity of the positive feedback current to a change in the tip–substrate distance.[24] The fitted topography plot yielded the flat glass surface as expected from AFM topography whereas the glass surface seemed rougher in the original plot of the final tip position owing to the overshoot of the tip approach beyond the threshold of ~$0.40i_{T,\infty}$ with a step size of ~20 nm. The negligible overshoot at the Au surface is attributed to a smaller step size of ~1 nm, which was required to detect the sudden enhancement of the tip current response by redox-mediated electron tunneling. Noticeably, the grooves of the intelligent topography plots are deeper than those in the AFM plots and are consistent with those estimated by cross-sectional SEM images (Figure 2C). Moreover, the final tip positions over the grooves (up to ~24.15 μm in Figure 6A) go below the positions of Au and glass surfaces (~24.05 μm in Figure 6B) owing to the penetration of the tip into the grooves, thereby representing the non-flat topography of the substrate.

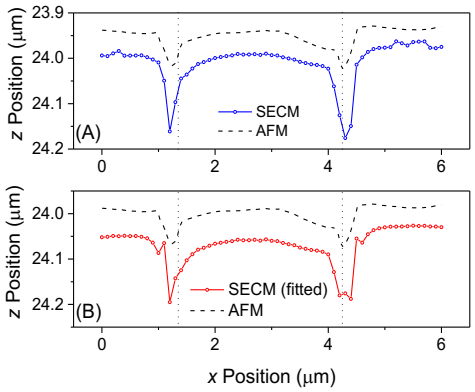

Figure 6. (A) The final z positions of tip approach from Figure 5 (blue circles) and (B) the z positions of substrate determined by fitting approach curves with theoretical or simulated curves (red circles). Dashed lines represent AFM topography from Figure 2D. Dotted lines represent the edge of Au band.

The intelligent mode yielded the topography-independent reactivity plot of the substrate as represented by the tip currents at the last points of approach curves (blue circles in Figure 7A). In addition, approach curves were fitted with theoretical curves (see below) to determine the tip current at the constant distance of d/a = 0.30, thereby yielding an ideal constant-distance reactivity plot (red circles in Figure 7A). The constant-distance plot of substrate reactivity is independent of the topography to show no groove, which is obvious from the complementary topography plot. Moreover, the constant-distance tip current is constant over the Au surface despite its asymmetric curvature. By contrast, the tip current during the constant-height line scan of the Au surface is not only enhanced but also varied (Figure 7B) to represent the convolution between the reactivity and topography of the curved Au surface. In addition, nanoscale grooves are unnoticed in the constant-height plot, where the tip current changes monotonically over the grooves owing to the convolution of topography with reactivity.

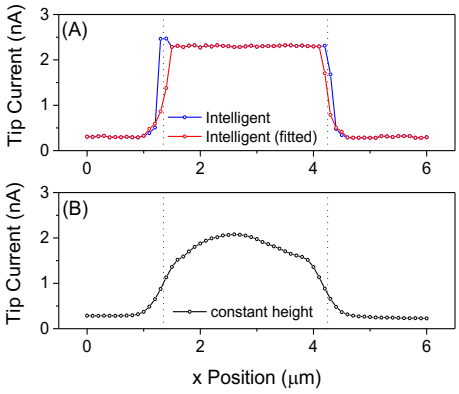

Figure 7. (A) The tip current at the last points of approach curves from Figure 5 (blue circles) or at a constant distance of $d/a = 0.30$ (red circles) as determined by fitting the approach curves with theoretical curves. Dotted lines represent the edge of Au band. (B) The tip current at the constant height. Dotted lines were positioned arbitrarily to represent the width of the Au band.

Characteristic Approach Curves. Five characteristic approach curves at the interdigitated Au electrodes were compared with theoretical curves to separately determine the actual position of the substrate surface under the tip for substrate topography (red circels in Figure 6B) and the tip currents at the constant distance from the local substrate surface for substrate reactivity (red circels in Figure 7A). Negative and positive approach curves at flat glass and Au surfaces fitted well with eqs S-1 and S-2 (Figure 8A) to represent the lowest and highest substrate reactivity, respectively. By contrast, both positive and negative feedback effects were observed when the tip approached the boundary between the edge of the Au band and the inert groove (Figure 8B). Specifically, the tip current gradually increased when the tip was still far from the boundary to experience a positive feedback effect from the Au band more than a negative feedback effect from the recessed groove. As the tip approached the boundary closer, the negative feedback effect became comparable to the positive feedback effect to reach a maximum tip current around the tip position of 23.84 μm. The negative feedback effect became dominant at shorter distances until the positive feedback effect from the side of the Au band became significant to eventually increase the tip current beyond the tip position of ~24.0 μm. The tip approach was terminated around ~24.2 μm, where the tip current increased abruptly owing to redox-mediated electron tunneling to satisfy eq 4. The final tip position was lower than the Au and glass surfaces (~24.05 μm in Figure 6B) to yield the penetration depth of ~150 nm, which is comparable to the groove depth of ~150 nm as estimated by SEM (Figure 2C). The penetration depth, however, is too large for the tip with an outer diameter of 0.78 μm. This result implises the tip–substarte contact, e.g., around 24.15 μm or even earlier, as indicated by the tip damage (Figure S-6).

The tip current was enhanced abruptly by redox-mediated electron tunneling also when the tip approached closer to the Au side of the boundary (Figure 8C). In this case, the positive feedback effect always exceeded the negative feedback effect to monotonically increase the tip current at the shorter distances until redox-mediated electron tunneling suddenly increased the tip current at extremely short distances to terminate the tip approach without contact. It should be noted that redox-mediated electron tunneling was observed also over the flat Au region when the tip approach was terminated not by employing the threshold of the positive feedback current (e.g., $i_T > 3.0 i_{T,\infty}$) but at a shorter tip–substrate distance by evaluating the slope of the positive approach curve (eq 4).

Importantly, the nanoscale grooves were manifested in the intelligent topography plot (Figure 6A) because a mild negative feedback effect was observed when the tip approached the inert groove adjacent to the Au band (Figure 8D). The experimental approach curve fitted well with an approach curve simulated for a tip approaching the inert groove to yield a more positive current than the diffusion-limited negative feedback current (eq S-2). Accordingly, the tip approached closer to the groove as represented in the intelligent topography plot (Figure 6A) until the tip approach was terminated by the tip–substrate contact (eq S-17) without reaching the threshold tip current of $0.4 i_{T,\infty}$. The contact can be prevented by the real-time fitting of the approach curve (eq S-16) while maintaining the close tip approach to the substrate.

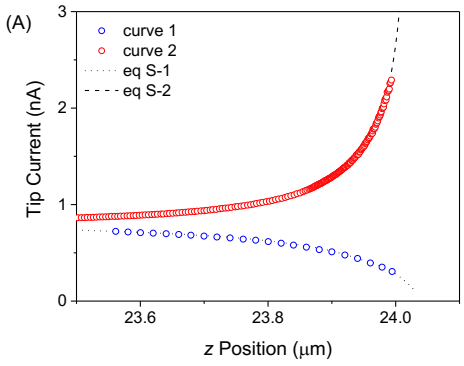

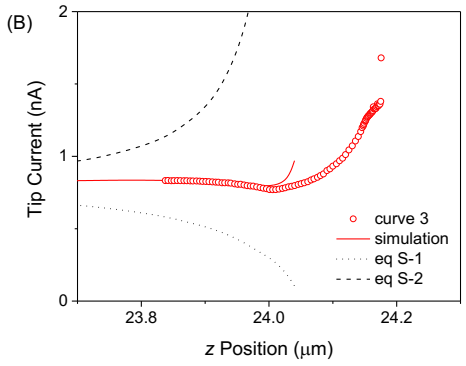

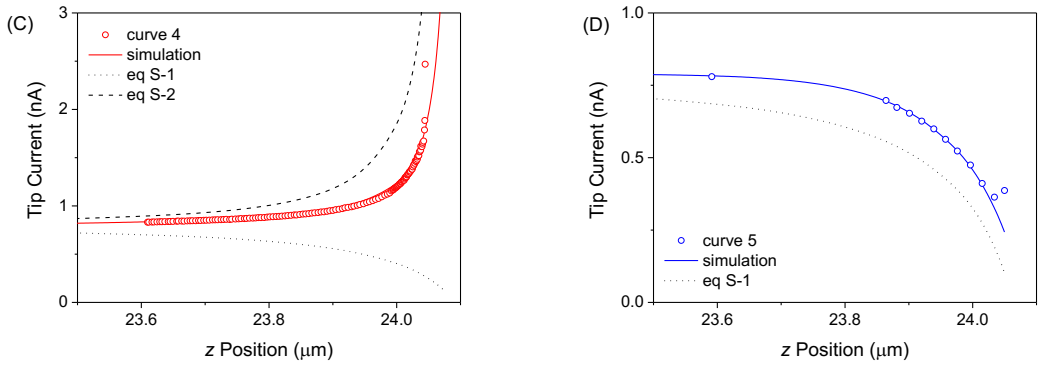

Figure 8. Experimental approach curves (circles) at (A) glass (blue) and Au (red) surfaces, (B) at the Au/glass boundary, and at (C) Au and (D) glass sides of the boundary in 10 mM $Ru(NH_3)_6^{3+}$ and 1 M KCl as adapted from Figure 5. Solid lines are simulated approach curves. Dotted and dashed lines represent diffusion-limited negative and positive approach curves, respectively.

Feedback Mechanism Based on Redox-Mediated Electron Tunneling. A sudden increase in the tip current (e.g., the last three data points of curve 4 in Figure 8C) was analyzed and attributed to long-range electron tunneling mediated by redox molecules. In this analysis, both experimental and simulated tip currents based only on the positive feedback effect (open circles and solid line, respectively, in Figure 9) changed linearly within the short distance range of only ~20 nm, which was measured by using a capacitive sensor of the piezo stage. Non-uniform step sizes between adjacent experimental points (0.9 ± 0.4 nm) are noticeable and due to the dynamic control of the piezo stage.[21]

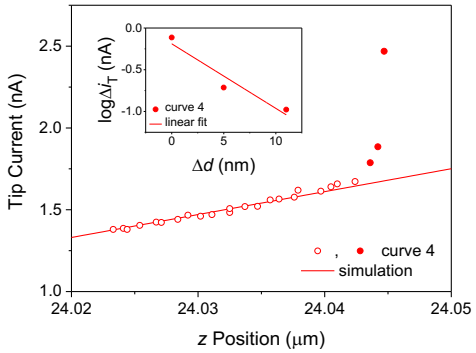

Figure 9. Experimental approach curve (circles) adapted from Figure 8C for the assessment of the tip current enhanced beyond the simulated positive feedback current fitted for the narrow distance range (red line). The inset shows the dependence of the additional tip current on a change in the tip–substrate distance.

Specifically, the tip current at the last three data points of curve 4 (closed circles in Figure 9) exceeded the expected positive feedback current (solid line) significantly to yield differences, $\Delta i_T(\Delta d)$, which were plotted against the corresponding changes in the tip–substrate distance, Δd, with respect to the last data point (closed circles in the inset). The plot shows an exponential distance-dependence of $\Delta i_T(\Delta d)$ as expected for solvent-mediated electron tunneling between the tip and the substrate,[25] which is equivalent to

$$\Delta i_T(\Delta d) = \Delta i_T(\Delta d = 0)\exp(-\beta\Delta d) \quad (5)$$

where a decay constant, β, of 0.18 $Å^{-1}$ was obtained from the best fit (solid line). This β value, however, is much smaller than experimental values of ~1 $Å^{-1}$ as determined by scanning tunneling microscopy (STM) in the aqueous electrolyte solution.[26] Moreover, when the atomic scale STM tip was positioned within ~1 nm from the conductive substrate, the resultant tunneling current increased exponentially by several orders of magnitude to reach the mA level, which far exceeds the low-nA level of the SECM tip current (Figure 9). The negligible contribution of solvent-mediated electron tunneling to the SECM tip current ensures that the short tip–substrate distance is still long enough to avoid the tip–substrate contact.

The distance-dependence of the enhanced SECM tip current over a short distance range of ~1 nm (closed circles in Figure 9 and its inset) is much weaker than expected for solvent-mediated electron tunneling (see above) and is attributed to long-range electron tunneling mediated by diffusing redox molecules. In this feedback mechanism, the weak distance dependence of the tip current originates from a distance-dependent standard electron-transfer rate constant, $k^0(\delta)$, as given by[20]

$$k^0(\delta) = k^0(\delta = 0)\exp(-\beta\delta) \quad (6)$$

where δ is the distance between a redox molecule and the tip (or the substrate) and $\delta = 0$ corresponds to the closest location of the redox molecule where electron transfer is possible, i.e., the outer Helmholtz plane for an outer-sphere redox couple.[27] Eq 6 implies that a fast redox molecule with a sufficiently large $k^0(\delta = 0)$ value can be completely depleted or regenerated even at $\delta > 0$ to thin a diffusion layer between the tip and the substrate. The resultant tip current response is larger than expected from the corresponding positive feedback current, where electron transfer is assumed to occur only at $\delta = 0$.[17] So far, redox-mediated electron tunneling in a nanogap cell with two electrodes has been proposed only theoretically.[20] Specifically, a pair of concentric spherical electrodes with various gap widths of ≤3 nm fully depleted or regenerated redox molecules with $k^0(\delta = 0) = 6 \times 10^8$ s^{-1} at δ = ~0.3 nm in the solution with $\beta = 1$ $Å^{-1}$. The simulated diffusion-limited current based on redox-mediated electron tunneling depended on the gap width much more weakly than expected for direct electron tunneling mediated by solvent molecules between the tip and the substrate.

It should be noted that a small step size of ~1 nm was needed (red circles in Figures 8A–8C) to detect a sudden increase in the tip response by redox-mediated electron tunneling, thereby lengthening

the measurement of positive approach curves. The time of approach curve measurement was minimized by employing a custom fuzzy logic algorithm,[28] which dramatically reduced the initial step size of 0.27 μm as the tip approached closer to the reactive region. This algorithm also enabled the faster measurement of negative approach curves with much larger step sizes of down to 20 nm (blue circles in Figures 8A and 8D).

Intelligent Reactivity and Topography Imaging. We employed the new algorithm (Figure 4) to demonstrate intelligent reactivity and topography imaging without the tip–substrate contact, which can damage the tip[16] (Figure S-6A) or the substrate[18] to potentially cause artifacts. The lack of tip–substrate contact was ensured after imaging by good fits between experimental and theoretical approach curves (e.g., Figure S-5) as well as by the lack of tip damage (Figure S-6B). After all approach curves were measured, intelligent reactivity and topography images of an interdigitated Au electrode (Figures 10A and 10B, respectively) were obtained by the fitting of each approach curve with a theoretical curve to separately determine the tip current at a constant distance of d/a = 0.3 and the location of the substrate under the tip as illustrated above (Figures 6B and 7A, respectively). The reactivity image demonstrates the highest tip currents for two Au bands and lowest tip currents for two glass regions as well as intermediate tip currents for boundaries (Figure 10A). The intelligent reactivity image ensures the uniformly high reactivity of the Au bands and the uniform inertness of the glass surface. The topography image (Figure 10B) demonstrates grooved boundaries between Au and glass surfaces as well as the diagonal tilt of the substrate from the lower corner at the left top to the higher corner at the right bottom. The tilt of the substrate distorts the constant-height image of the interdigitated Au electrodes (Figure 10C) to show higher tip current at the right band than at the left band as well as along each band from the top to the bottom, thereby yielding the highest tip current at the bottom of the right band. The highest tip current in the constant-height image appears as a "hot spot," which is disproved by the intelligent reactivity image and is attributed to the tilt of the substrate by the intelligent topography image.

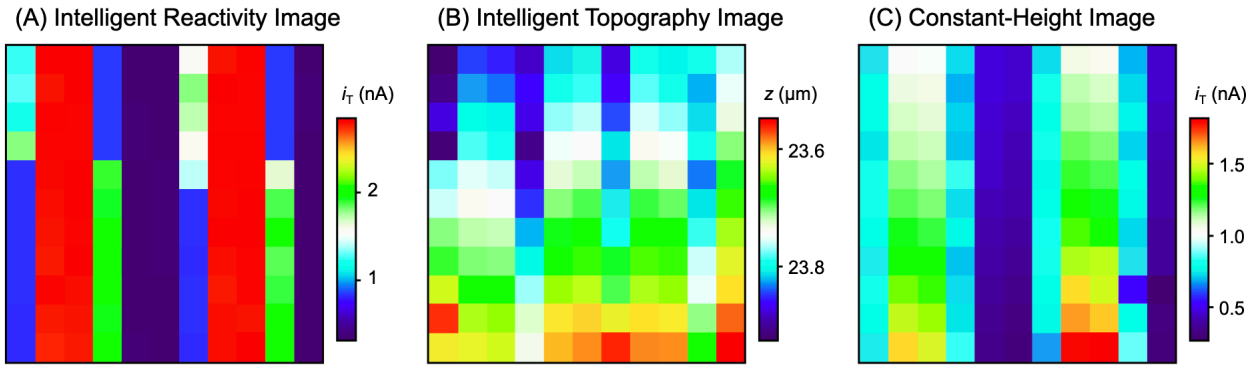

Figure 10. Intelligent (A) reactivity and (B) topography images and (C) constant-height image of 2.8 μm-wide Au bands embedded in a grooved glass substrate in 10 mM $Ru(NH_3)_6^{3+}$ and 1 M KCl. Each pixel is equivalent to 1 μm × 1 μm. The tip was scanned laterally from the left bottom corner and stepped upward after each line scan. The outer and inner tip radii of 0.44 μm and 0.28 μm, respectively, were determined by SEM.

Importantly, intelligent images of the interdigitated electrodes are based on the feedback mechanisms without redox-mediated electron tunneling to quantitatively represent the reactivity and topography of the substrates. The tip current enhanced by redox-mediated electron tunneling was used only for the termination of the tip approach and was excluded during the post-imaging fit of approach curves (e.g., Figure 8C). By contrast, the tip current enhanced by solvent-mediated electron tunneling was used in a recent study to separately image the substrate topography from the substrate reactivity, which was imaged in the feedback mode at a longer distance.[29] The combination of SECM with STM requires a conductive substrate in contrast to the intelligent mode based only on the SECM feedback mechanisms. Moreover, distinguishment between feedback and tunneling currents is challenging in the constant-height mode. Recently, the constant-height image of single nanoparticles was analyzed quantitatively to find that the edges of the cubic nanoparticles were too sharp in the experimental constant-height images to fit the hemispherical images of the nanoparticles simulated with the positive feedback mode, where the edges were blurred by the diffusion of a redox mediator.[30] This discrepancy was attributed to the contribution of solvent-mediated tunneling current to the tip response, which questions whether similar images of single spherical nanoparticles based on the same experimental approach in the prior work[31] resulted from the SECM feedback effect to represent the reactivity of the nanoparticles or from tunneling current to represent their conductivity. This ambiguity is an intrinsic limitation of nanoscale constant-height imaging.

The time required for intelligent imaging (30 minutes for the measurement of 121 approach curves in Figures 10A and 10B) is intrinsically longer owing to the repeated measurement and assessment of many approach curves. The imaging time, however, can be shortened by employing a faster tip-positioning system,[29] a smaller tip, and a faster and more sophisticated computing hardware for the analysis of approach curves as discussed in Supporting Information.

CONCLUSIONS

In this work, we developed the intelligent mode of nanoscale SECM imaging to simultaneously obtain separate reactivity and topography images of non-flat substrates with both reactive and inert regions. This powerful imaging mode will advance SECM imaging of single nanostructures such as molecular transport through single nanopores,[4,5] electrocatalysis at single nanoparticles,[6,7] and beyond. In the intelligent mode, the post-analysis of each approach curve constituted a quantitative topography image and a topography-independent reactivity image. Remarkably, intelligent topography imaging revealed nanoscale grooves adjacent to a Au band as quantitatively as SEM and AFM, which contain no reactivity information. The nanoscale grooves were not noticeable in the constant-height

SECM image owing to the convolution of substrate reactivity with substrate topography, which includes the tilt of the substrate. The intelligent reactivity image traced a continuous change in the constant-distance tip current at the boundary between reactive and inter regions, which prevents the constant-current imaging.[9] The intelligent mode was applied to substartes with diffusion-limited reactivities under purely positive and negative feedback conditions in this study but will be applicable to substartes with any reactivity by employing the corresponding general theory[23] (eq S-5) to guide non-contact tip approach.

The numerical post-analysis of approach curves in the intelligent mode enabled us to assess imaging mechanisms and experimentally propose the feedback mechanism based on long-range electron tunneling mediated by redox molecules. Our observations support the theoretical prediction that redox-mediated electron tunneling is manifested at intermediate tip–substrate distances that are longer than required for solvent-mediated electron tunneling but are shorter than the distances where traditional feedback effects are dominant.[20] This new feedback mechanism was useful for intelligent imaging to enable non-contact tip positioning at a short distance from the vertical Au edge. By contrast, redox-mediated electron tunneling was not reported in a recent SECM study, where the tip current was controlled by traditional feedback effects and then by solvent-mediated electron tunneling to yield an expected decay constant of ~1 $Å^{-1}$ when a tip approached an unbiased metal nanoparticle on the inert substrate.[32] More work is needed by using biased substrates to voltammetrically assess the feedback mechanism based on redox-mediated electron tunneling, where the distance-dependence is highly and uniquely sensitive to the substrate potential[20] in comparison with solvent-mediated electron tunneling.[26]

ASSOCIATED CONTENT

Supporting Information

The Supporting Information is available free of charge on the ACS Publications website.

Prevention of electrostatic tip damage, theoretical approach curves, finite element simulation, non-contact measurement of approach curves, nanotip damage with substrate contact, and imaging time (PDF)

AUTHOR INFORMATION

Corresponding Author

* S. Amemiya. E-mail: amemiya@pitt.edu. Fax: 412-624-8611.
* K. C. Leonard. E-mail: kcleonard@ku.edu. Fax: 785-864-4967.

Author Contributions

D.T.J. and R.J.B. equally contributed to this work.

ACKNOWLEDGMENT

This work was supported by the Army Research Office Young Investigator Grant No. 66446-CH-YIP (Award Number W911NF-17-1-0098). S.A. acknowledges supports from the National Science Foundation (CHE-1904258) and the National Institutes of Health (R01 GM112656). We thank Prof. Joaquín Rodríguez-López for his comment on the effect of electron tunneling on the tip current

REFERENCES

(1) Amemiya, S., Nanoscale scanning electrochemical microscopy. In *Electroanalytical chemistry*, Bard, A. J.; Zoski, C. G., Eds. CRC Press: 2015; pp 1–72.

(2) Kai, T.; Zoski, C. G.; Bard, A. J. Scanning electrochemical microscopy at the nanometer level. *Chem. Commun.* **2018**, *54*, 1934–1947.

(3) Kwak, J.; Bard, A. J. Scanning electrochemical microscopy. Apparatus and two-dimensional scans of conductive and insulating substrates. *Anal. Chem.* **1989**, *61*, 1794–1799.

(4) Shen, M.; Ishimatsu, R.; Kim, J.; Amemiya, S. Quantitative imaging of ion transport through single nanopores by high-resolution scanning electrochemical microscopy. *J. Am. Chem. Soc.* **2012**, *134*, 9856–9859.

(5) Chen, R.; Balla, R. J.; Lima, A.; Amemiya, S. Characterization of nanopipet-supported ITIES tips for scanning electrochemical microscopy of single solid-state nanopores. *Anal. Chem.* **2017**, *89*, 9946–9952.

(6) Kim, J.; Renault, C.; Nioradze, N.; Arroyo-Currás, N.; Leonard, K. C.; Bard, A. J. Electrocatalytic activity of individual Pt nanoparticles studied by nanoscale scanning electrochemical microscopy. *J. Am. Chem. Soc.* **2016**, *138*, 8560–8568.

(7) Kim, J.; Renault, C.; Nioradze, N.; Arroyo-Currás, N.; Leonard, K. C.; Bard, A. J. Nanometer scale scanning electrochemical microscopy instrumentation. *Anal. Chem.* **2016**, *88*, 10284–10289.

(8) Amemiya, S.; Guo, J.; Xiong, H.; Gross, D. A. Biological applications of scanning electrochemical microscopy: Chemical imaging of single living cell and beyond. *Anal. Bioanal. Chem.* **2006**, *386*, 458–471.

(9) Wipf, D. O.; Bard, A. J.; Tallman, D. E. Scanning electrochemical microscopy. 21. Constant-current imaging with an autoswitching controller. *Anal. Chem.* **1993**, *65*, 1373–1377.

(10) Fan, F.-R. F.; Bard, A. J. Imaging biological macromolecules on mica in humid air by scanning electrochemical microscopy. *Proc. Natl. Acad. Soci. U.S.A.* **1999**, *96*, 14222–14227.

(11) Laforge, F. O.; Velmurugan, J.; Wang, Y.; Mirkin, M. V. Nanoscale imaging of surface topography and reactivity with the scanning electrochemical microscope. *Anal. Chem.* **2009**, *81*, 3143–3150.

(12) O'Connell, M. A.; Wain, A. J. Combined electrochemical-topographical imaging: A critical review. *Anal. Methods* **2015**, *7*, 6983–6999.

(13) Lazenby, R. A.; McKelvey, K.; Unwin, P. R. Hopping intermittent contact-scanning electrochemical microscopy (HIC-SECM): Visualizing interfacial reactions and fluxes from surfaces to bulk solution. *Anal. Chem.* **2013**, *85*, 2937–2944.

(14) Derylo, M. A.; Morton, K. C.; Baker, L. A. Parylene insulated probes for scanning electrochemical–atomic force microscopy. *Langmuir* **2011**, *27*, 13925–13930.

(15) Morris, C. A.; Chen, C.-C.; Baker, L. A. Transport of redox probes through single pores measured by scanning electrochemical-scanning ion conductance microscopy (SECM–SICM). *Analyst* **2012**, 2933–2938.

(16) Balla, R. J.; Jantz, D. T.; Kurapati, N.; Chen, R.; Leonard, K. C.; Amemiya, S. Nanoscale intelligent imaging based on real-time analysis of approach curve by scanning electrochemical microscopy. *Anal. Chem.* **2019**, *91*, 10227–10235.

(17) Bard, A. J.; Mirkin, M. V.; Unwin, P. R.; Wipf, D. O. Scanning electrochemical microscopy. 12. Theory and experiment of the feedback mode with finite heterogeneous electron-transfer kinetics and arbitrary substrate size. *J. Phys. Chem.* **1992**, *96*, 1861–1868.

(18) Lazenby, R.; McKelvey, K.; Peruffo, M.; Baghdadi, M.; Unwin, P. R. Nanoscale intermittent contact-scanning electrochemical microscopy. *J. Solid State Electrochem.* **2013**, *17*, 2979–2987.

(19) Jedraszko, J.; Michalak, M.; Jönsson-Niedziolka, M.; Nogala, W. Hopping mode SECM imaging of redox activity in ionic liquid with glass-coated inlaid platinum nanoelectrodes prepared using a heating coil puller. *J. Electroanal. Chem.* **2018**, *815*, 231–237.

(20) White, R. J.; White, H. S. Electrochemistry in nanometer-wide electrochemical cells. *Langmuir* **2008**, *24*, 2850–2855.

(21) Kim, J.; Shen, M.; Nioradze, N.; Amemiya, S. Stabilizing nanometer scale tip-to-substrate gaps in scanning electrochemical

microscopy using an isothermal chamber for thermal drift suppression. *Anal. Chem.* **2012**, *84*, 3489–3492.

(22) Shen, J.; Zhang, D.; Zhang, F.-H.; Gan, Y. AFM tip-sample convolution effects for cylinder protrusions. *Appl. Surf. Sci.* **2017**, *422*, 482–491.

(23) Lefrou, C.; Cornut, R. Analytical expressions for quantitative scanning electrochemical microscopy (SECM). *ChemPhysChem* **2010**, *11*, 547–556.

(24) Wei, C.; Bard, A. J. Scanning electrochemical microscopy XXIX. In situ monitoring of thickness changes of thin films on electrodes. *J. Electrochem. Soc.* **1995**, *142*, 2523–2527.

(25) Pan, J.; Jing, T. W.; Lindsay, S. M. Tunneling barriers in electrochemical scanning tunneling microscopy. *J. Phys. Chem.* **1994**, *98*, 4205–4208.

(26) Hugelmann, M.; Schindler, W. In situ distance tunneling spectroscopy at Au(111)/0.02 M $HClO_4$. *J. Electrochem. Soc.* **2004**, *151*, E97–E101.

(27) Klymenko, O. V.; Svir, I.; Amatore, C. Molecular electrochemistry and electrocatalysis: A dynamic view. *Mol. Phys.* **2014**, *112*, 1273–1283.

(28) Barforoush, J. M.; McDonald, T. D.; Desai, T. A.; Widrig, D.; Bayer, C.; Brown, M. K.; Cummings, L. C.; Leonard, K. C. Intelligent scanning electrochemical microscopy tip and substrate control utilizing fuzzy logic. *Electrochim. Acta* **2016**, *190*, 713–719.

(29) Edmondson, J. F.; Meloni, G. N.; Costantini, G.; Unwin, P. R. Synchronous electrical conductance- and electron tunnelling-scanning electrochemical microscopy measurements. *ChemElectroChem* **2020**, *7*, 697–706.

(30) Blanchard, P.-Y.; Sun, T.; Yu, Y.; Wei, Z.; Matsui, H.; Mirkin, M. V. Scanning electrochemical microscopy study of permeability of a thiolated aryl multilayer and imaging of single nanocubes anchored to it. *Langmuir* **2016**, *32*, 2500–2508.

(31) Sun, T.; Yu, Y.; Zacher, B. J.; Mirkin, M. V. Scanning electrochemical microscopy of individual catalytic nanoparticles. *Angew. Chem. Int. Ed.* **2014**, *53*, 14120–14123.

(32) Sun, T.; Wang, D.; Mirkin, M. V. Tunneling mode of scanning electrochemical microscopy: Probing electrochemical processes at single nanoparticles. *Angew. Chem. Int. Ed.* **2018**, *57*, 7463–7467.

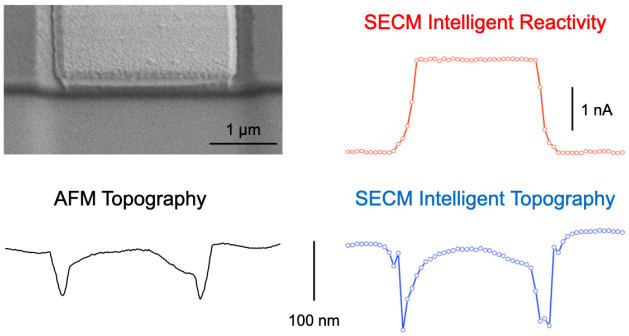
1 µm
SECM Intelligent Reactivity
1 nA
AFM Topography
SECM Intelligent Topography
100 nm